

Learning Disease-Sensitive Latent Interaction Graphs From Noisy Cardiac Flow Measurements

Viraj Patel¹, Marko Grujic³, Philipp Aigner³, Theodor Abart³, Marcus Granegger³, Deblina Bhattacharjee¹, and Katharine Fraser²

¹ Department of Computer Science, University of Bath, Bath, BA2 7AY, UK
{vbp24, db2466}@bath.ac.uk

² Department of Mechanical Engineering, University of Bath, Bath, BA2 7AY, UK
khf27@bath.ac.uk

³ Christian Doppler Laboratory for Mechanical Circulatory Support, Department of Cardiac and Thoracic Aortic Surgery, Medical University of Vienna, Vienna, Austria
<first-name>.<last-name>@meduniwien.ac.at

Abstract. Cardiac blood flow patterns contain rich information about disease severity and clinical interventions, yet current imaging and computational methods fail to capture underlying relational structures of coherent flow features. We propose a physics-informed, latent relational framework to model cardiac vortices as interacting nodes in a graph. Our model combines a neural relational inference architecture with physics-inspired interaction energy and birth-death dynamics, yielding a latent graph sensitive to disease severity and intervention level. We first apply this to computational fluid dynamics simulations of aortic coarctation. Learned latent graphs reveal that as the aortic radius narrows, vortex interactions become stronger and more frequent. This leads to a higher graph entropy, correlating monotonically with coarctation severity ($R^2 = 0.78$, Spearman $|\rho| = 0.96$). We then extend this method to ultrasound datasets of left ventricles under varying levels of left ventricular assist device support. Again the latent graph representation captures the weakening of coherent vortical structures, thereby demonstrating cross-modal generalisation. Results show latent interaction graphs and entropy serve as robust and interpretable markers of cardiac disease and intervention.

Keywords: Vortex Dynamics · Ultrasound Imaging · Neural Relational Inference

1 Background and Motivation

1.1 Introduction

Cardiovascular disease is the leading cause of death globally, and expected to increase [5]. Coarctation of the aorta (CoA), a narrowing of the aorta, is the most commonly misdiagnosed congenital heart disease in prenatal screening, though echocardiographic markers may improve detection rates [8]. Issues inherent to

echocardiography, like speckle noise and suboptimal Doppler angles, may cause underestimation of the severity of CoA [2]. Additionally, anatomical defects can be subtle in prenatal screening and can often mask pressure gradients and flow rate abnormalities [29]. Patients with repaired CoA may develop left ventricular (LV) dysfunction with age, thus regular monitoring of the LV function is recommended from infancy through adulthood [2]. When intervention is required, a left ventricular assist device (LVAD) may be implanted [13]. From prenatal screenings, to the implant of LVADs into patients, echocardiography plays a crucial role in diagnosis and monitoring.

Although denoising and despeckling of ultrasound images have been widely studied using both classical and deep learning approaches [16, 22], suboptimal scanning angles and occlusions remain difficult to recover [21]. Flow fields provide more sensitive functional information than raw images and are increasingly used in echocardiography, yet remain susceptible to noise, out-of-plane motion, and complex dynamics [1, 4, 28]. While physics-informed reconstruction methods partially mitigate these issues, many deep models are still sensitive to ultrasound artefacts [23]. An alternative is to represent flow structurally rather than pixel-wise. In particular, Gabriel graphs have been used to construct scale-invariant representations in which nodes correspond to critical points, like vortices, encoding the geometric organisation of the flow without relying on dense image information [20, 26, 27]. Clinically, subtle and evolving defects demand such robust representations: coarctation of the aorta induces vortex rings and disturbed secondary flows [12, 14, 17], while left ventricular vortex (LVV) dynamics are closely linked to cardiac function and LVAD support, as ventricular contractility and device assistance alter vortex formation time, circulation strength, spatial organisation, and persistence within the ventricle [1, 9, 24]. These phenomena motivate modelling the evolution and interaction of critical points and vortices through graph-based, scale-invariant representations of the flow.

We present a model that learns a scale invariant, noise-robust, physics-informed graph-based representation of various flow conditions. The main contributions are: (1) A neural relational inference model with a physics-head that learns disease-sensitive graph representations of cardiovascular flows, (2) The entropy of this learned representation as a quantitative marker that is sensitive to disease severity with strong monotonicity and statistical significance, (3) Validation of this model and marker across computational fluid dynamics (CFD) datasets of CoA and real ultrasound scans of a heart under LVAD support.

1.2 Neural Relational Inference

Given an interacting system of N entities, let $\mathbf{x}_i^{(t)} \in \mathbb{R}^d$ be the feature vector of entity $i \in \{1, \dots, N\}$ at timestep t . Neural Relational Inference (NRI) is an encoder-decoder architecture that learns a latent graph representation of the interacting system from a set of trajectories $\mathbf{x}_i = (\mathbf{x}_i^1, \dots, \mathbf{x}_i^T)$ [19]. In particular, the encoder is formalised by

$$q_\phi(\mathbf{z}|\mathbf{x}) = \prod_{i \neq j} q_\phi(\mathbf{z}_{ij}|\mathbf{x}), \quad (1)$$

where $\mathbf{z}_{ij} \in \mathbb{R}^{n_e}$ is the latent interaction vector between entities i and j . This is trained with the decoder, $p_\theta(\mathbf{x}|\mathbf{z})$, to jointly optimise the ELBO

$$\mathcal{L}(\phi, \theta) = \mathbb{E}_{q_\phi} [\log p_\theta(\mathbf{x}|\mathbf{z})] - \text{KL}[q_\phi(\mathbf{z}|\mathbf{x})||p(\mathbf{z})], \quad (2)$$

where the first term minimises trajectory reconstruction error, and the second term ensures \mathbf{z}_{ij} are meaningful. NRI has been proven effective on a wide range of problems, from physics simulations to protein interactions [32]. Many modifications have been made to the original NRI architecture; notably dynamic NRI proposed by Graber et al. [11] learned time-varying interactions $\mathbf{z}_{ij}(t)$. Yang et al. [31] applied NRI to reinforcement learning problems and multi-agent systems, but found that current NRI architectures rely on the assumption that all interacting entities in the system are present at every timestep throughout the recorded trajectories. They expressed the need for a model that could account for missing data and the birth and death of an entity. In addition to this strong assumption, NRI has yet to be adapted for systems with variable cardinality. When trained on datasets with many instances of a system, it is assumed that each instance has the same number of interacting entities.

2 Method

2.1 Data Preparation

Flow Field Acquisition Initially, flow field data was obtained from a 3D CFD simulation of pulsatile flow through an aortic geometry [18]. Coarctation was modeled by narrowing a fixed region of the descending aorta, with severity defined as the percentage of the original radius (e.g. 40% indicates the narrowed radius is 40% of the baseline). To emulate ultrasound Echo-PIV conditions, a 2D cross-section was extracted with in-plane velocity projection, and multiplicative Rayleigh noise ($\sigma = 5, 10$) was added [15]. Additionally, LVAD data was acquired from an ex vivo mock circulatory loop using the explanted heart of a 55kg female sheep. The pulmonary vein, aorta, and pulmonary artery were connected to controlled reservoirs to regulate preload, afterload (Windkessel analogue), and coronary outflow, enabling simulation of varying LVAD support modes. Following configuration of support level, imaging was performed using a GE 6Vc-D echocardiographic probe. Echo-PIV is an ultrasound-based velocimetry technique that evaluates blood flow fields by tracking contrast microbubbles between successive image frames. In this study, microbubbles ($\sim 10\mu\text{m}$ diameter) were injected into the bloodstream and their displacement was calculated via cross-correlation to generate 2D velocity vector fields [6].

Vortex Tracking Once 2D flow fields were obtained, vortices were identified in each frame using the SWIRL algorithm [3], which applies the Rortex criterion to isolate rigid-body rotation while excluding shear effects, making it more robust than conventional swirling strength or vorticity methods for 2D flows. For each frame, a feature vector $\mathbf{x}_i^{(t)}$ (including the coordinate of centre, radius, orientation, existence $\in \{0, 1\}$, and vorticity) of each vortex were recorded and compared between consecutive frames. Vortices in neighbouring

frames that overlapped spatially, and had the same orientation, were considered to be the same vortex recorded at different timesteps. Trajectory data for all detected vortices were assembled into a single tensor, with zero-filled features at timesteps where a vortex was absent. As in [19], all features were scaled to the range $[-1, 1]$.

2.2 Latent Interaction Model

Building on the original NRI architecture [19], several modifications were introduced to address the limitations outlined in Section 1.2 (Figure 1, orange). A physics head g_E was incorporated to encode circulation energy between vortices, and a conditioning network g_s was added to account for coarctation severity and LVAD support level. To accommodate variable vortex cardinality, a masked loss function was implemented during training. The latent relational structure retained two edge types (interaction/no interaction) with prior probabilities of 0.3 and 0.7, respectively.

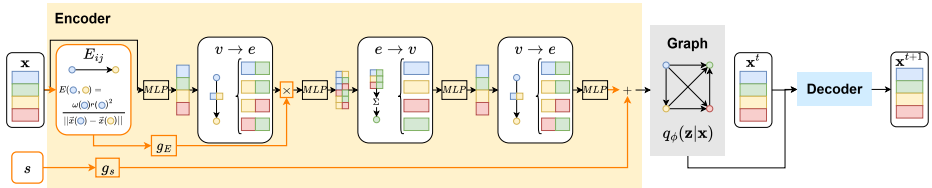


Fig. 1: NRI architecture, with modifications compared with [19] in orange. The encoder, which used a disease severity conditioned physics head, and decoder, are alternating MLPs and message passing layers. Solid blocks represent node-level embeddings and multi-coloured blocks represent edge-level embeddings.

Energy Gating For each pair of vortices, a proxy for the circulation energy inspired by the Biot-Savart Law [25] was calculated

$$E_{ij} = \frac{\omega_i r_i^2}{\|\mathbf{x}_i - \mathbf{x}_j\|_2}, \quad (3)$$

where ω_i , r_i , and \mathbf{x}_i are the vorticity, radius, and 2D coordinates of the centre of the i th vortex, respectively. This was chosen to be asymmetric to reflect the directed latent graph induced by temporal ordering. A single layer perceptron g_E was used to map this interaction energy to the latent edge space. This allowed the encoder to learn how strongly the strength of the physical interaction should influence the inferred relational structure, rather than imposing a hard physical constraint.

Conditioning on Severity The variable s was used to encode severity. For the CoA dataset, this was the level of coarctation taking in a range of 30-100. For the supported left ventricle, this was the level of support provided by the LVAD,

with 0 indicating no support, 0.5 indicating partial support, and 1 indicating full support. A linear layer g_s conditioned the encoder on this severity and the result was multiplied by the logits output by the encoder, before being converted into the probability distribution q_ϕ . This conditioning allowed for sensitivity of s on the resulting latent interaction graph, without explicitly learning s .

Temporal Consistency and Masked Loss The original NRI model used a placeholder for an adjacency matrix that prevents self-loops in the resulting latent graph [19]. In our model, the entities were ordered by time of birth, and the graph placeholder ensured that later vortices could not have a causal effect on an earlier vortex, preserving temporal consistency. Due to a mixture of continuous and discrete features, different activation functions and loss functions were used to reconstruct each feature. We first define $x_o \in \{0, 1\}^3$ as the one-hot encoded orientation and $x_e \in \{0, 1\}$ as the binary value to determine if the vortex exists at a particular time. Given a feature vector $\mathbf{x} \in \mathbb{R}^8$, we define $\tilde{\mathbf{x}} := \mathbf{x} \setminus \{x_o, x_e\} \in \mathbb{R}^4$ as the vector of all continuous features. The reconstruction loss was masked by existence and defined as

$$\mathcal{L}_{\text{rec}} = (\mathbb{E}_{q_\phi} [\log p_\theta(\tilde{\mathbf{x}}|\mathbf{z})] + CE(\hat{x}_o, x_o))x_e, \quad (4)$$

where $CE(\cdot, \cdot)$ is the cross-entropy and \hat{x}_o is the predicted orientation from the decoder. An existence loss $\mathcal{L}_{\text{exist}} = BCE(\hat{x}_e, x_e)$, where $BCE(\cdot, \cdot)$ is the binary cross entropy and \hat{x}_e is the predicted value of existence from the decoder, was added to ensure that the model accurately predicted when a vortex exists. The total loss

$$\mathcal{L} = \mathcal{L}_{\text{rec}} - \lambda_{KL} KL[q_\phi(\mathbf{z}|\mathbf{x})||p(\mathbf{z})] + \mathcal{L}_{\text{exist}} \quad (5)$$

was jointly optimised by annealing λ_{KL} from 0 to 1 during the course of training.

2.3 Implementation

For fair comparison, the same training setup, including the train-test split ratio, proposed by Kipf et al. [19] was used for this work. The CoA dataset contained 48 simulations, with 40 simulations used for training and 8 simulations used for testing and validation. The dataset was balanced such that each coarctation level and noise level was represented by the same number of simulations. The LVAD dataset contained 26 scans, with 18 scans used for training and 8 used for evaluating the performance of the model. This dataset contained 10 samples of no support, 8 samples of partial support, and 8 samples of full support. All instances of the model were trained on a NVIDIA GeForce RTX 3090 GPU with 24GB memory. The original NRI model was used as a baseline, with the performance of the model determined by the quality of reconstruction and the clinical significance of the resultant representation. The quality of reconstruction was measured by the mean squared error (MSE), as in [19], and mean absolute error (MAE) for all features except existence, which was measured by prediction accuracy. To measure the significance of the latent interaction graphs, with each edge-type treated as separate graphs, the entropy H of each was computed and

correlated with severity variable s . The p -value from Spearman correlation was recorded, in addition to a monotonicity (the fraction of consecutive severity-level pairs where entropy changes in the expected direction) score and the R^2 value of a least squares regressor between H and s . Ethical approval from the relevant animal welfare committee was obtained prior to performing any experiments. The dataset and code will be released upon acceptance.

3 Results and Discussion

3.1 CFD: Aortic Coarctation

To ensure performance was independent of parameter initialisation, the model was trained 5 times and mean and variance of each metric recorded. The existence accuracy (0.7882) and trajectory MSE (0.0166) were masked to avoid considering padded vortices. This MSE is low considering the range of the trajectory data, with small variance (7.06×10^{-6}). The model predicted when vortices exist with high accuracy, and reconstructed trajectories retained a shape similar to the ground truth, albeit with some scaling and sign issues. Then the latent representation captured the structural patterns of the underlying vortex dynamics, with less emphasis on the exact trajectory magnitudes.

The distribution of probabilities assigned to the interaction edge-type varies with coarctation level (Fig. 2a): as the severity of the disease increases, the probability mass shifts toward stronger interactions, yielding an increase in latent graph entropy (Fig. 2a). The Spearman correlation coefficient of -0.9553 was consistent with this trend, with a highly significant p -value (9.92×10^{-4}). Graph entropy explains a substantial proportion of disease severity variance ($R^2 = 0.7774$), indicating increasing interaction complexity as a dominant and systematic marker of disease progression rather than a weak or incidental correlation. This trend is explained by the underlying flow physics: as coarctation severity increases, the flow transitions toward more complex secondary structures, leading to a greater number and strength of vortex-vortex interactions. The relationship between entropy and radius is strongest when the radius is 60% or smaller (Fig. 2b), likely because stronger confinement produces persistent wall-induced vortex interactions that increase coherence in the learned edge probabilities [7].

3.2 Ultrasound: LVAD Supported Ventricle

When extended to ultrasound scans of an LVAD supported left ventricle, the existence accuracy and MSE of the reconstructed trajectories were 0.7604 and 0.0039 respectively. In contrast with the CoA dataset, the reconstruction maintained the same sign as the ground truth data but suffered similar scaling issues. The model’s prediction of vortex existence timing aligned almost perfectly with the ground truth.

When investigating the latent representation, it was found that the first edge type, corresponding to no causal interaction, was more indicative of the change

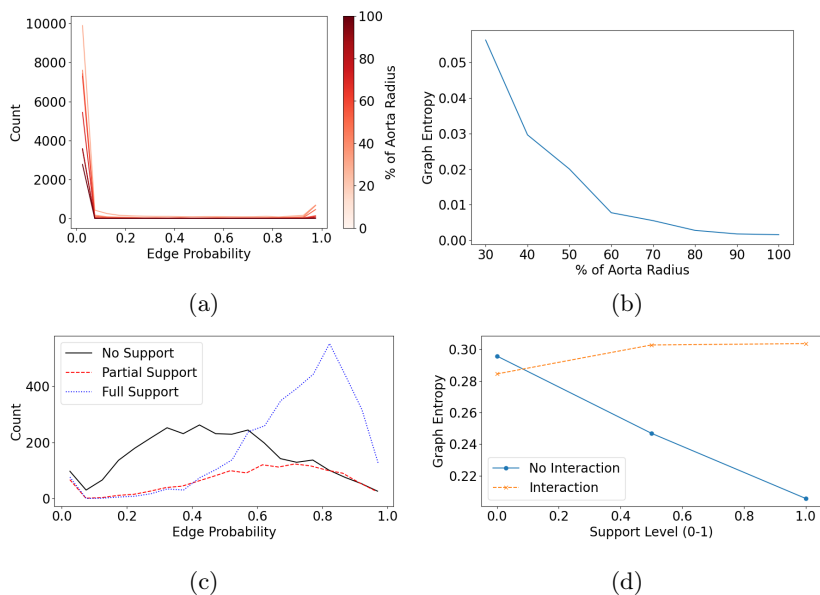


Fig. 2: Aortic coarctation: (a) the distribution of edge probability and (b) the entropy of the latent interaction graph changes with coarctation level. LVAD support: (c) the distribution of edge probability (for no interaction) and (d) the entropy of the latent interaction graph changes with LVAD support level. Decreasing % of aorta radius corresponds to increasing disease severity. LVAD support levels: 0.0 = no support, 0.5 = partial support, and 1.0 = full support.

in flow conditions. In particular, as the support level increases, the distribution of edge weights skews to higher values with lower variance (Fig. 2c). This is in agreement with the decrease in entropy of the non-interaction latent graph with increasing support level (monotonicity score of 1.0, Fig. 2d). Spearman correlation produced a coefficient of -0.9449 with a $p = 0.0004$, and $R^2 = 0.8549$. These results imply that as the support level increased, many vortex pairs become consistently non-interacting and the model becomes increasingly confident about this across different scans. In contrast to the non-interaction graph, the entropy of the interaction graph increases between no support and partial support, but plateaus between partial and full support (Fig. 2d). This suggests a transitional regime in which residual vortex interactions weaken before stabilising or disappearing at higher support. This can be explained by competing inflow-outflow pathways: natural filling ejects flow through the aortic valve, whereas full support redirects it towards the apex [30], and partial support strips vorticity into diffuse, less coherent structures [10].

3.3 Ablations

Our full model achieves the lowest MAE, reflecting improved average reconstruction of vortex trajectories, while the ablation with no severity conditioning

has slightly higher MAE but lower MSE, indicating fewer extreme deviations (Table 1 reports best of 5 training runs; mean results given in Sec. 3.1). Ablations reveal that vortex ordering improved existence accuracy and reconstruction by providing temporal context for vortex births. Moreover, physics gating enhanced the latent representation by incorporating circulation energy constraints that capture physically meaningful interactions. Finally, severity conditioning allowed the model to specialise across disease levels, producing representations that more accurately reflect the flow alterations induced by coarctation.

Table 1: Ablations on NRI model applied to CoA dataset.

Ablation	Existence Accuracy	MAE	MSE	ρ	p -value	R^2	Monotonicity
None	0.840	0.013	0.015	-0.988	4.26×10^{-6}	0.915	1.00
No ordering	0.605	0.014	0.015	-0.691	0.058	0.845	0.800
No physics gating	0.778	0.014	0.016	-0.167	0.693	0.000	0.640
No severity conditioning	0.704	0.013	0.011	0.518	0.188	0.418	0.308
Original NRI	0.617	0.016	0.019	0.458	0.254	0.210	0.308

To further verify that severity conditioning does not introduce a trivial $s \rightarrow H$ mapping, we performed a perturbation analysis: for each CoA simulation, s was varied by ± 10 and the resulting change in entropy ΔH was recorded. The sensitivity is strongly state-dependent: ΔH is largest at severe coarctation (30-40% radius) and diminishes to near zero at mild levels (80-100%), confirming that the conditioning modulates the encoder’s response to flow features rather than memorising a fixed mapping.

3.4 Limitations and Future Work

The datasets used in this study remain modest in size and external validation on independent cohorts is required to establish generalisability. In particular, varying the size and shape of the aortic geometry and obtaining echocardiograms from other test subjects would increase confidence in our results. Furthermore, the current setup with binary edge types may oversimplify subtle interactions, since vortex coupling strength is continuous in reality.

4 Conclusion

We introduced a noise-robust, physics-informed neural relational inference framework to characterise vortex interaction structure in altered cardiovascular flow conditions, including coarctation of the aorta and LVAD-supported left ventricular flow. By analysing the entropy of inferred edge types, we identified systematic changes in relational uncertainty associated with increasing vascular obstruction severity and mechanical support. In coarctation, relational entropy captured progressive disruption of flow structures as the aortic radius narrowed. In the LVAD setting, decreasing entropy of the non-interaction edge type alongside a transient increase in interaction entropy suggested a transitional regime at intermediate support levels, reflecting competition between native pulsatile dynamics and

pump-driven flow. Together, these results demonstrate that relational modelling provides a compact and interpretable representation of complex haemodynamic flow structures, highlighting its potential as a general framework for studying pathological cardiovascular flow.

References

1. Aigner, P. et al.: Ventricular Flow Field Visualization During Mechanical Circulatory Support in the Assisted Isolated Beating Heart. *Ann Biomed Eng* **48**(2), 794–804 (Feb 2020). <https://doi.org/10.1007/s10439-019-02406-x>
2. Bhatt, A.B. et al.: Isolated Coarctation of the Aorta: Current Concepts and Perspectives. *Front. Cardiovasc. Med.* **9** (May 2022). <https://doi.org/10.3389/fcvm.2022.817866>
3. Canivete Cuissa, J.R., Steiner, O.: Innovative and automated method for vortex identification. I. Description of the SWIRL algorithm. *Astronomy and Astrophysics* **668**, A118 (Dec 2022). <https://doi.org/10.1051/0004-6361/202243740>
4. Cantinotti, M. et al.: Characterization of Aortic Flow Patterns by High-Frame-Rate Blood Speckle Tracking Echocardiography in Children. *Journal of the American Heart Association* **12**(8), e026335 (Apr 2023). <https://doi.org/10.1161/JAHA.122.026335>
5. Chong, B. et al.: Global burden of cardiovascular diseases: Projections from 2025 to 2050. *Eur. J. Prev. Cardiol.* **32**(11), 1001–1015 (Aug 2025). <https://doi.org/10.1093/eurjpc/zwae281>
6. Crapper, M., Bruce, T., Gouble, C.: Flow field visualization of sediment-laden flow using ultrasonic imaging. *Dynamics of Atmospheres and Oceans* **31**(1-4), 233–245 (2000)
7. Danaila, I. et al.: Formation number of confined vortex rings. *Phys. Rev. Fluids* **3**(9), 094701 (Sep 2018). <https://doi.org/10.1103/PhysRevFluids.3.094701>
8. Dijkema, E.J., Leiner, T., Grotenhuis, H.B.: Diagnosis, imaging and clinical management of aortic coarctation. *Heart* **103**(15), 1148–1155 (Aug 2017). <https://doi.org/10.1136/heartjnl-2017-311173>
9. Gharib, M. et al.: Optimal vortex formation as an index of cardiac health. *Proceedings of the National Academy of Sciences* **103**(16), 6305–6308 (2006)
10. Ghodrati, M. et al.: Validation of numerically simulated ventricular flow patterns during left ventricular assist device support. *Int J Artif Organs* **44**(1), 30–38 (Jan 2021). <https://doi.org/10.1177/0391398820904056>
11. Graber, C., Schwing, A.G.: Dynamic Neural Relational Inference. In: *Proceedings of the IEEE/CVF Conference on Computer Vision and Pattern Recognition*. pp. 8513–8522 (2020)
12. Gülan, U. et al.: Experimental study of aortic flow in the ascending aorta via Particle Tracking Velocimetry. *Exp Fluids* **53**(5), 1469–1485 (Nov 2012). <https://doi.org/10.1007/s00348-012-1371-8>
13. Hamad, E.A. et al.: LVAD therapy as a catalyst to heart failure remission and myocardial recovery. *Clinical Cardiology* **46**(10), 1154–1162 (2023). <https://doi.org/10.1002/clc.24094>
14. Hope, M.D. et al.: Clinical evaluation of aortic coarctation with 4D flow MR imaging. *Journal of Magnetic Resonance Imaging* **31**(3), 711–718 (2010). <https://doi.org/10.1002/jmri.22083>

15. Karaođlu, O., Bilge, H.Ş., Uluer, İ.: Removal of speckle noises from ultrasound images using five different deep learning networks. *Engineering Science and Technology, an International Journal* **29**, 101030 (May 2022). <https://doi.org/10.1016/j.jestch.2021.06.010>
16. Kaur, A., Dong, G.: A Complete Review on Image Denoising Techniques for Medical Images. *Neural Process Lett* **55**(6), 7807–7850 (Dec 2023). <https://doi.org/10.1007/s11063-023-11286-1>
17. Keshavarz-Motamed, Z. et al.: Effect of coarctation of the aorta and bicuspid aortic valve on flow dynamics and turbulence in the aorta using particle image velocimetry. *Exp Fluids* **55**(3), 1696 (Mar 2014). <https://doi.org/10.1007/s00348-014-1696-6>
18. Khan, O.: AortaPINNsData (Jan 2025)
19. Kipf, T. et al.: Neural Relational Inference for Interacting Systems. In: *Proceedings of the 35th International Conference on Machine Learning*. pp. 2688–2697. PMLR (Jul 2018)
20. Krueger, P.S. et al.: Quantitative classification of vortical flows based on topological features using graph matching. *Proc. A* **475**(2228), 20180897 (Aug 2019). <https://doi.org/10.1098/rspa.2018.0897>
21. Osmanski, B.F. et al.: Ultrafast Doppler Imaging of Blood Flow Dynamics in the Myocardium. *IEEE Transactions on Medical Imaging* **31**(8), 1661–1668 (Aug 2012). <https://doi.org/10.1109/TMI.2012.2203316>
22. Palhano Xavier de Fontes, F. et al.: Real time ultrasound image denoising. *J Real-Time Image Proc* **6**(1), 15–22 (Mar 2011). <https://doi.org/10.1007/s11554-010-0158-5>
23. Patel, V., Kreusser, L., Fraser, K.: Dynamic Reconstruction of Ultrasound-Derived Flow Fields With Physics-Informed Neural Fields (Nov 2025). <https://doi.org/10.48550/arXiv.2511.01804>
24. Pedrizzetti, G., Domenichini, F.: Nature Optimizes the Swirling Flow in the Human Left Ventricle. *Phys. Rev. Lett.* **95**(10), 108101 (Sep 2005). <https://doi.org/10.1103/PhysRevLett.95.108101>
25. Perry, A.E., Chong, M.S.: Topology of flow patterns in vortex motions and turbulence. *Appl. Sci. Res.* **53**(3), 357–374 (Dec 1994). <https://doi.org/10.1007/BF00849110>
26. Reza-Soltani, e. et al.: The role of artificial intelligence and machine learning in cardiovascular imaging and diagnosis. *Cureus* **16**(9) (2024)
27. Tobak, M., Peake, D.J.: Topology of three-dimensional separated flows. *Tech. Rep. A-8554* (Apr 1981)
28. Vignon-Clementel, I.D.: *Écoulement Intraventriculaire En Echocardiographie Doppler Avec Réseaux de Neurones Fondés Sur La Physique*. Ph.D. thesis, INSA Lyon (2024)
29. Villalain, C. et al.: Diagnostic accuracy of prenatal ultrasound in coarctation of aorta: Systematic review and individual participant data meta-analysis. *Ultrasound in Obstetrics & Gynecology* **63**(4), 446–456 (2024). <https://doi.org/10.1002/uog.27576>
30. Wong, K. et al.: Intraventricular flow patterns and stasis in the LVAD-assisted heart. *Journal of Biomechanics* **47**(6), 1485–1494 (Apr 2014). <https://doi.org/10.1016/j.jbiomech.2013.12.031>
31. Yang, Y. et al.: Behavior-Inspired Neural Networks for Relational Inference (Mar 2025). <https://doi.org/10.48550/arXiv.2406.14746>

32. Zhu, J. et al.: Neural relational inference to learn long-range allosteric interactions in proteins from molecular dynamics simulations. *Nat Commun* **13**(1), 1661 (Mar 2022). <https://doi.org/10.1038/s41467-022-29331-3>